

AN EFFICIENT CUMULATIVE EDGE-DETECTION METHOD FOR IMAGE RECONSTRUCTION

TOLUWANI OKUNOLA*, MIRJETA PASHA†, AND MISHA E. KILMER‡

Abstract. When reconstructing images from noisy measurements, such as in medical scans or scientific imaging, we face an inverse problem: recovering an unknown image from indirect, corrupted observations. These problems are typically ill-posed, meaning small amounts of noise can lead to inaccurate reconstructions. Regularization techniques address this by incorporating prior assumptions about the solution, such as smoothness or sparsity. However, standard methods often blur sharp edges—the boundaries between tissues or structures—losing critical detail.

A powerful strategy for edge preservation is iterative reweighting, which solves a sequence of weighted subproblems with adaptively updated weights. Non-cumulative schemes derive weights from the current iterate alone and can be solved efficiently using the Recycled Majorization-Minimization Generalized Krylov Subspace method (RMM-GKS). The cumulative approach of Gazzola et al. progressively accumulates edge information across iterations, achieving superior edge preservation but at high computational cost.

This work introduces CR- ℓ_q -RMM-GKS, which combines cumulative edge detection with computational efficiency. We integrate Gazzola’s cumulative weighting with RMM-GKS, which handles general ℓ_q penalties ($0 < q \leq 2$), automatically selects regularization parameters, and recycles Krylov subspaces between iterations, reducing the nested structure to two levels.

Numerical experiments in signal deblurring and tomography demonstrate that CR- ℓ_q -RMM-GKS produces significantly sharper edge reconstructions than standard non-cumulative methods. In particular, CR- ℓ_1 -RMM-GKS outperforms both standard ℓ_1 methods and CR- ℓ_2 -RMM-GKS, indicating that cumulative weighting and ℓ_1 penalties are highly complementary.

Key words. edge preservation, Krylov subspace methods, iterative regularization, inverse problems.

AMS subject classifications. 65F22, 65F10, 65K10, 68U10.

1. Introduction. In many scientific and medical imaging applications—from computed tomography (CT) to astronomical imaging—we aim to reconstruct an underlying image $\mathbf{x}_{\text{true}} \in \mathbb{R}^n$ from indirect, noisy measurements $\mathbf{b} \in \mathbb{R}^m$ [10]. The linear forward problem is

$$(1.1) \quad \mathbf{b} = \mathbf{A}\mathbf{x}_{\text{true}} + \boldsymbol{\eta},$$

where $\mathbf{A} \in \mathbb{R}^{m \times n}$ (with $m \geq n$ in the overdetermined setting; underdetermined cases such as sparse-angle tomography are also accommodated), represents the forward imaging model and $\boldsymbol{\eta} \in \mathbb{R}^m$ is additive noise. A key challenge is that \mathbf{A} is typically severely ill-conditioned, with singular values that decay rapidly toward zero. This means that small perturbations in the data \mathbf{b} —even tiny amounts of noise—can cause massive changes in the solution. Consequently, the naive least-squares solution, $\arg \min_{\mathbf{x}} \|\mathbf{A}\mathbf{x} - \mathbf{b}\|_2^2$, amplifies noise dramatically and produces unusable reconstructions.

To obtain a stable and meaningful solution, we must employ *regularization*, which incorporates prior knowledge or assumptions about the desired solution \mathbf{x}_{true} . One of the most well-known regularization methods is Tikhonov regularization, which solves

$$(1.2) \quad \mathbf{x}_\lambda = \arg \min_{\mathbf{x}} \left\{ \|\mathbf{A}\mathbf{x} - \mathbf{b}\|_2^2 + \lambda \|\mathbf{L}\mathbf{x}\|_2^2 \right\}.$$

*Department of Mathematics, Tufts University (toluwani.okunola@tufts.edu)

†Department of Mathematics, Virginia Tech (mpasha@vt.edu)

‡Department of Mathematics, Tufts University (misha.kilmer@tufts.edu)

Here, $\lambda > 0$ is the regularization parameter balancing data fidelity and regularization, and \mathbf{L} is typically a discrete gradient or derivative operator. The regularization term $\|\mathbf{L}\mathbf{x}\|_2^2$ penalizes large values in $\mathbf{L}\mathbf{x}$, which correspond to sharp changes in pixel intensities. This promotes smoothness throughout the image, effectively suppressing noise in regions that should be uniform.

However, sharp intensity changes are also exactly what occur at *edges*—the boundaries between different structures, tissues, or materials that carry crucial diagnostic or scientific information. As illustrated in Figure 1.1, both true edges and noise produce large gradient values. Standard ℓ_2 regularization cannot distinguish between them and therefore applies uniform smoothing indiscriminately, blurring critical structural details. Preserving edges while suppressing noise is therefore a central challenge in image reconstruction.

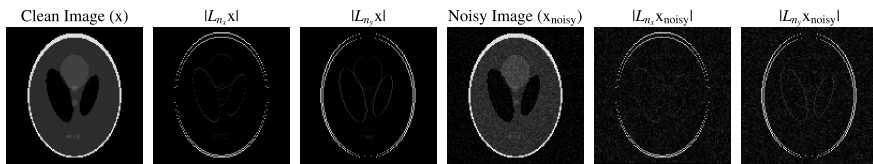


Fig. 1.1: Visualizing the effect of the discrete gradient operator \mathbf{L} . From left to right: a clean image, its horizontal and vertical gradient magnitudes, a noisy version, and its gradient magnitudes. Both actual edges and noise contribute to large gradient values, complicating edge preservation in standard ℓ_2 regularization.

1.1. Edge-Preserving Regularization via Iterative Reweighting. To overcome the edge-blurring limitation of standard Tikhonov regularization, a powerful general strategy has emerged: *iterative reweighting*. The core idea is to solve a sequence of weighted ℓ_2 subproblems, where the weights are updated to adapt the penalty to the structure of the evolving solution. By assigning smaller weights at detected edge locations and larger weights elsewhere, these methods can preserve edges while still regularizing smooth regions.

Iterative reweighting schemes differ primarily in *how the weights are computed*, leading to two major classes:

Non-cumulative weighting. The most widely used approach derives weights from the *current iterate alone* [2, 4, 6, 21]. A particularly successful example uses ℓ_q -norm penalties ($0 < q < 2$), most commonly $q = 1$ as in Total Variation (TV) regularization [20]. Since the ℓ_1 -norm is non-smooth, Majorization-Minimization (MM) methods [12, 14, 19] convert it into a sequence of weighted ℓ_2 subproblems. Modern solvers such as the Recycled Majorization-Minimization Generalized Krylov Subspace (RMM-GKS) method [17] achieve impressive computational efficiency by recycling Krylov subspaces across iterations and automatically selecting regularization parameters. Operator-splitting approaches such as Split Bregman / ADMM [8, 3] also solve TV-type problems efficiently but require a different algorithmic infrastructure (dual variable updates, parameter tuning for the augmented Lagrangian) and do not naturally accommodate the Krylov recycling strategy central to our framework.

Cumulative weighting. A fundamentally different philosophy, introduced by Gazdola et al. [7], updates weights by *accumulating* edge information across iterations. Rather than discarding the edge detection history, their method builds weights that

progressively “remember” previously identified edges through a multiplicative update mechanism. This cumulative strategy excels at preserving fine structures and produces superior edge quality compared to non-cumulative methods. However, the method requires solving multiple nested optimization problems at each step, making it computationally expensive for large-scale problems.

1.2. Contribution. This work bridges the gap between computational efficiency and edge preservation quality by introducing *Cumulative Reweighted ℓ_q Regularization with Recycled Majorization-Minimization Generalized Krylov Subspace* (CR- ℓ_q -RMM-GKS). Our framework combines the cumulative edge-detection strategy of Gazzola et al. [7] with the computational efficiency of the RMM-GKS solver [17], which handles general ℓ_q -norm penalties ($0 < q \leq 2$), automatically selects regularization parameters, and recycles Krylov subspaces between outer iterations. In this respect, our approach is related to hybrid Krylov methods [5] that combine iterative projection with automatic parameter selection, but extends this paradigm to cumulative ℓ_q reweighting with subspace recycling across outer iterations.

At each outer iteration, we update cumulative weights and pass the modified regularization operator to RMM-GKS, which warm-starts from the Krylov subspace constructed in the previous iteration. This reduces the deeply nested structure of prior cumulative methods to two levels while extending cumulative weighting to general ℓ_q penalties. The resulting method solves

$$\mathbf{x}^{(\ell)} = \arg \min_{\mathbf{x}} \left\{ \|\mathbf{A}\mathbf{x} - \mathbf{b}\|_2^2 + \lambda_\ell \|\mathbf{D}^{(\ell)}\mathbf{L}\mathbf{x}\|_q^q \right\}, \quad 0 < q \leq 2,$$

where each subproblem benefits from both automatic parameter selection and subspace recycling.

Numerical experiments on 1D deblurring and challenging sparse-angle tomography demonstrate that CR- ℓ_q -RMM-GKS achieves significantly sharper edge preservation and higher reconstruction quality than standard non-cumulative methods, with convergence speeds competitive with or faster than non-cumulative solvers. Notably, CR- ℓ_1 -RMM-GKS outperforms CR- ℓ_2 -RMM-GKS in both edge quality and convergence speed, demonstrating that cumulative weighting and ℓ_1 penalties are highly complementary strategies.

The remainder of the paper is organized as follows. Section 2 reviews necessary background including cumulative reweighting, MM methods, and the RMM-GKS solver. Section 3 presents the CR- ℓ_q -RMM-GKS algorithm in detail. Section 4 reports numerical results, and Section 5 concludes the paper.

2. Background and Related Work. This section reviews the mathematical operators and algorithmic components underlying our proposed method.

2.1. Discrete Gradient Operator. For a 2D image of size $n_x \times n_y$, we use the discrete gradient operator $\mathbf{L} \in \mathbb{R}^{2n_x n_y \times n_x n_y}$ constructed via Kronecker products:

$$\mathbf{L} = \begin{bmatrix} \mathbf{L}_{n_x} \otimes \mathbf{I}_{n_y} \\ \mathbf{I}_{n_x} \otimes \mathbf{L}_{n_y} \end{bmatrix},$$

where \mathbf{L}_{n_x} and \mathbf{L}_{n_y} are first-order finite difference operators with homogeneous Neumann boundary conditions. For 1D signals, we use \mathbf{L}_n directly. The operator $\mathbf{L}\mathbf{x}$ approximates the image gradient at each pixel.

2.2. ℓ_q -Norm Regularization and Majorization-Minimization. The generalized ℓ_q -norm regularization problem ($0 < q \leq 2$) is:

$$(2.1) \quad \min_{\mathbf{x}} J(\mathbf{x}) = \|\mathbf{Ax} - \mathbf{b}\|_2^2 + \lambda \|\mathbf{Lx}\|_q^q.$$

When $q = 1$ (Total Variation-like penalty), the ℓ_1 -norm promotes sparse gradients and preserves sharp edges more effectively than ℓ_2 . For $q \leq 1$, the ℓ_q -norm is non-differentiable, and for $q < 1$ it becomes non-convex, making direct optimization challenging.

The Majorization-Minimization (MM) principle [12, 6] addresses this by iteratively transforming the non-smooth problem into a sequence of weighted ℓ_2 problems:

$$(2.2) \quad \mathbf{x}^{(k+1)} = \arg \min_{\mathbf{x}} \left\{ \|\mathbf{Ax} - \mathbf{b}\|_2^2 + \lambda \|\mathbf{W}^{(k)} \mathbf{Lx}\|_2^2 \right\}.$$

Here, $\mathbf{W}^{(k)}$ is a diagonal weighting matrix derived from the current solution $\mathbf{x}^{(k)}$. Unlike the cumulative weights discussed in Section 2.4, MM weights are *non-cumulative*—they depend only on the current iterate and do not accumulate edge information across iterations.

2.3. Recycled MM-GKS Solver. The Majorization-Minimization Generalized Krylov Subspace (MM-GKS) framework [11, 16, 17] efficiently solves ℓ_q -regularized problems (2.1) by combining:

1. Majorization of the non-smooth ℓ_q term into weighted ℓ_2 subproblems,
2. Projection onto a generalized Krylov subspace,
3. Automatic regularization parameter selection (e.g., discrepancy principle, L-curve) within the projected problem.

At each iteration, MM-GKS generates weights via majorization, projects the resulting weighted problem onto a low-dimensional Krylov subspace (making the problem tractable), automatically selects the regularization parameter on the small projected system, and expands the subspace using the residual. Importantly, projection and parameter selection occur within a *single iteration loop*—avoiding the nested structure of earlier projection methods.

Subspace Recycling. For large-scale problems, repeated Krylov expansions can become expensive. Recycled MM-GKS (RMM-GKS) [17] improves efficiency through an *enlarge-compress* strategy: expand the Krylov subspace from dimension k_{\min} to k_{\max} to improve the solution, then compress back to k_{\min} by retaining only the most informative directions. This bounds memory growth and reduces matrix-vector products. Crucially, the compressed subspace is *reused* to warm-start the next outer iteration, providing computational memory between successive solves. Algorithm 2.1 summarizes the approach.

2.4. Cumulative Reweighted ℓ_2 Regularization. Cumulative reweighting [7] enhances Tikhonov regularization by adaptively modifying spatial weights across outer iterations. At outer iteration ℓ , it solves:

$$(2.3) \quad \mathbf{x}^{(\ell)} = \arg \min_{\mathbf{x}} \left\{ \|\mathbf{Ax} - \mathbf{b}\|_2^2 + \lambda_{\ell} \|\mathbf{D}^{(\ell)} \mathbf{Lx}\|_2^2 \right\}.$$

Here, $\mathbf{D}^{(\ell)} = \text{diag}(\mathbf{d}^{(\ell)})$ is a diagonal weighting matrix updated cumulatively via

$$(2.4) \quad \mathbf{g}^{(\ell-1)} = \frac{|\mathbf{D}^{(\ell-1)} \mathbf{Lx}^{(\ell-1)}|}{\|\mathbf{D}^{(\ell-1)} \mathbf{Lx}^{(\ell-1)}\|_{\infty}}, \quad \mathbf{d}^{(\ell)} = \mathbf{d}^{(\ell-1)} \circ (1 - \mathbf{g}^{(\ell-1)})^{\circ s},$$

Algorithm 2.1 RMM-GKS: Recycled Majorization-Minimization Generalized Krylov Subspace Method

Require: $\mathbf{A} \in \mathbb{R}^{m \times n}$, $\mathbf{L} \in \mathbb{R}^{p \times n}$, $\mathbf{b} \in \mathbb{R}^m$, $q \in (0, 2]$, $k_{\min} < k_{\max}$, $\epsilon > 0$, initial subspace $\mathbf{V}_0 \in \mathbb{R}^{n \times k_{\min}}$

Ensure: Solution \mathbf{x} , parameter λ , recycled subspace \mathbf{V}

1: Initialize $\mathbf{x}^{(1,0)} = \mathbf{0}$, $\mathbf{V} \leftarrow \mathbf{V}_0$, $\lambda^{(1,0)} = 0$

2: Compute initial MM weights: $\mathbf{W}^{(1,0)} = \text{diag}\left(\left(\|\mathbf{L}\mathbf{x}^{(1,0)}\|^2 + \epsilon^2\right)^{(q-2)/2}\right)$

3: **for** $i = 1, 2, \dots$ until convergence **do**

4: **ENLARGE:** Expand subspace from k_{\min} to k_{\max}

5: **for** $j = 0, 1, \dots, k_{\max} - k_{\min} - 1$ **do**

6: Compute residual gradient:

$$\mathbf{r}^{(i,j)} = \mathbf{A}^T(\mathbf{A}\mathbf{x}^{(i,j)} - \mathbf{b}) + \lambda^{(i,j)}\mathbf{L}^T(\mathbf{W}^{(i,j)})^2\mathbf{L}\mathbf{x}^{(i,j)}$$

7: Expand subspace: $\mathbf{V} \leftarrow [\mathbf{V}, \mathbf{r}^{(i,j)} / \|\mathbf{r}^{(i,j)}\|_2]$

8: Select $\lambda^{(i,j)}$ via discrepancy principle [1] or L-curve [9] and solve projected problem:

$$\mathbf{z}^{(i,j+1)} = \arg \min_{\mathbf{z}} \left\{ \|\mathbf{A}\mathbf{V}\mathbf{z} - \mathbf{b}\|_2^2 + \lambda^{(i,j)} \|\mathbf{W}^{(i,j)}\mathbf{L}\mathbf{V}\mathbf{z}\|_2^2 \right\}$$

9: Update solution: $\mathbf{x}^{(i,j+1)} = \mathbf{V}\mathbf{z}^{(i,j+1)}$

10: Update MM weights: $\mathbf{W}^{(i,j+1)} = \text{diag}\left(\left(\|\mathbf{L}\mathbf{x}^{(i,j+1)}\|^2 + \epsilon^2\right)^{(q-2)/2}\right)$

11: **end for**

12: **COMPRESS:** Retain k_{\min} most informative directions via SVD (see [17]):
 $\mathbf{V} \leftarrow \mathbf{V}\mathbf{M}$

13: Orthogonalize current solution and append to subspace:

$$\mathbf{v}_{\text{new}} = \frac{\mathbf{x}^{(i, k_{\max} - k_{\min})} - \mathbf{V}\mathbf{V}^T\mathbf{x}^{(i, k_{\max} - k_{\min})}}{\|\mathbf{x}^{(i, k_{\max} - k_{\min})} - \mathbf{V}\mathbf{V}^T\mathbf{x}^{(i, k_{\max} - k_{\min})}\|_2}, \quad \mathbf{V} \leftarrow [\mathbf{V}, \mathbf{v}_{\text{new}}]$$

14: **if** $\|\mathbf{x}^{(i, k_{\max} - k_{\min})} - \mathbf{x}^{(i-1, k_{\max} - k_{\min})}\|_2 / \|\mathbf{x}^{(i-1, k_{\max} - k_{\min})}\|_2 < \text{tol}$ **then**

15: **break**

16: **end if**

17: Set $\mathbf{x}^{(i+1,0)} \leftarrow \mathbf{x}^{(i, k_{\max} - k_{\min})}$, $\lambda^{(i+1,0)} \leftarrow \lambda^{(i, k_{\max} - k_{\min} - 1)}$, $\mathbf{W}^{(i+1,0)} \leftarrow \mathbf{W}^{(i, k_{\max} - k_{\min})}$

18: **end for**

19: **return** $\mathbf{x}^{(i, k_{\max} - k_{\min})}$, $\lambda^{(i, k_{\max} - k_{\min} - 1)}$, \mathbf{V}

where $s > 0$ is a smoothness parameter, $|\cdot|$ denotes element-wise absolute value, and $^{\circ s}$ denotes element-wise exponentiation. The normalized weighted gradient $\mathbf{g}^{(\ell-1)}$ reveals newly detected edges (components near 1) and previously detected edges or smooth regions (components near 0). The multiplicative update in (2.4) ensures that once an edge is detected, its associated penalty weight is progressively reduced and “remembered” across iterations, preventing re-smoothing and leading to robust edge preservation.

2.5. Joint Bidiagonalization for General-Form Tikhonov Problems. Each subproblem in (2.3) is a large-scale general-form Tikhonov problem: $\min_{\mathbf{x}} \|\mathbf{A}\mathbf{x} - \mathbf{b}\|_2^2 +$

$\lambda \|\tilde{\mathbf{L}}\mathbf{x}\|_2^2$, where $\tilde{\mathbf{L}} = \mathbf{D}^{(\ell)}\mathbf{L}$. Kilmer et al. [13] proposed solving such problems via a projection method based on joint bidiagonalization of $(\mathbf{A}, \tilde{\mathbf{L}})$. This iteratively constructs a small Krylov subspace \mathbf{Z}_k onto which the problem is projected, reducing it to a smaller system:

$$\min_{\mathbf{w} \in \mathbb{R}^k} \left\| \begin{bmatrix} \mathbf{A}\mathbf{Z}_k \\ \sqrt{\lambda}\tilde{\mathbf{L}}\mathbf{Z}_k \end{bmatrix} \mathbf{w} - \begin{bmatrix} \mathbf{b} \\ \mathbf{0} \end{bmatrix} \right\|_2^2.$$

Three-Level Nested Iteration. A key drawback of this method, especially when embedded within a cumulative reweighting scheme, is its deeply nested iterative structure. Generating each new basis vector for \mathbf{Z}_k requires an inner LSQR iteration to compute orthogonal projections. Moreover, the Krylov subspace \mathbf{Z}_k is typically rebuilt from scratch at each outer cumulative reweighting step (when $\mathbf{D}^{(\ell)}$ is updated). This leads to *three nested levels of iteration*:

1. outer cumulative weight update ($\mathbf{D}^{(\ell)}$ update),
2. middle-level joint bidiagonalization loop (Krylov subspace expansion),
3. inner LSQR iterations for orthogonal projections.

This deep nesting is computationally expensive and lacks “memory” between outer reweighting iterations, as subspaces are not recycled.

3. Cumulative Reweighted ℓ_q Regularization with Subspace Recycling.

Two complementary strategies underpin our method: **Cumulative reweighting** (Section 2.4) excels at edge preservation by accumulating edge information across iterations, but results in expensive nested iterations. **RMM-GKS** (Section 2.3) efficiently solves ℓ_q -regularized problems with automatic parameter selection and subspace recycling, but uses non-cumulative weights that discard edge detection history.

Our contribution integrates cumulative edge tracking with the computational efficiency of RMM-GKS. The key insight is that RMM-GKS can naturally accommodate the changing regularization operator $\mathbf{D}^{(\ell)}\mathbf{L}$ at each outer iteration by warm-starting from the recycled subspace, eliminating nested iterations while preserving cumulative edge detection.

3.1. Proposed Method. We propose *CR- ℓ_q -RMM-GKS* (Cumulative Reweighted ℓ_q Regularization with Recycled MM-GKS), which at outer iteration $\ell = 1, 2, \dots, N_{\text{out}}$ solves

$$(3.1) \quad \mathbf{x}^{(\ell)} = \arg \min_{\mathbf{x}} \left\{ \|\mathbf{A}\mathbf{x} - \mathbf{b}\|_2^2 + \lambda_\ell \|\mathbf{D}^{(\ell)}\mathbf{L}\mathbf{x}\|_q^q \right\}, \quad 0 < q \leq 2,$$

where the cumulative diagonal weight matrix $\mathbf{D}^{(\ell)} = \text{diag}(\mathbf{d}^{(\ell)})$ is updated via (2.4). Each subproblem is solved using RMM-GKS (Algorithm 2.1), which: (1) applies MM to convert the ℓ_q problem into weighted ℓ_2 subproblems, (2) projects onto a Krylov subspace initialized from the previous outer iteration, (3) automatically selects λ_ℓ via discrepancy principle or L-curve, and (4) returns the solution $\mathbf{x}^{(\ell)}$ and a compressed subspace $\mathbf{V}^{(\ell)}$ for recycling.

This approach offers key advantages:

1. **Reduced iteration depth:** two levels (outer cumulative update + inner RMM-GKS) instead of three.
2. **Subspace recycling** across outer iterations, dramatically reducing cost.
3. **Flexibility:** supports general ℓ_q penalties ($0 < q \leq 2$), not just ℓ_2 .
4. **Automatic parameter selection** via discrepancy principle or L-curve.
5. **Cumulative edge preservation** quality matching Gazzola et al.’s approach in [7].

Remark (Convergence Properties). Within each outer iteration ℓ , the cumulative weights $\mathbf{D}^{(\ell)}$ are fixed, so RMM-GKS solves a well-posed weighted ℓ_q problem of the form (3.1). The MM principle guarantees that each inner iterate is a descent step on the majorizing surrogate, and the discrepancy principle provides a principled stopping criterion for the inner solve. Across outer iterations, the multiplicative structure of (2.4) ensures that detected edge weights are monotonically non-increasing: once $\mathbf{d}^{(\ell)}$ is reduced, no subsequent update can increase it. This provides a form of one-sided monotonicity for the weight sequence. A full convergence theory for the outer cumulative loop remains open and is left for future work.

3.2. Algorithm. Algorithm 3.1 presents the complete method. The outer loop updates cumulative weights to progressively identify and preserve edges, while RMM-GKS (Line 4) warm-starts from the recycled subspace $\mathbf{V}^{(\ell-1)}$.

Algorithm 3.1 CR- ℓ_q -RMM-GKS: Cumulative Reweighted ℓ_q Regularization

Require: $\mathbf{A} \in \mathbb{R}^{m \times n}$, $\mathbf{L} \in \mathbb{R}^{p \times n}$, $\mathbf{b} \in \mathbb{R}^m$, $q \in (0, 2]$, N_{out} , k_{\min}, k_{\max} , $s > 0$, ϵ

Ensure: Solution $\mathbf{x}^{(N_{\text{out}})}$

- 1: Initialize: $\mathbf{x}^{(0)} = \mathbf{0}$, $\mathbf{d}^{(1)} = \mathbf{1} \in \mathbb{R}^p$, $\mathbf{V}^{(0)} \in \mathbb{R}^{n \times k_{\min}}$
 - 2: **for** $\ell = 1, 2, \dots, N_{\text{out}}$ **do**
 - 3: $\tilde{\mathbf{L}} = \text{diag}(\mathbf{d}^{(\ell)})\mathbf{L}$
 - 4: $[\mathbf{x}^{(\ell)}, \lambda_\ell, \mathbf{V}^{(\ell)}] = \text{RMM-GKS}(\mathbf{A}, \tilde{\mathbf{L}}, \mathbf{b}, q, k_{\min}, k_{\max}, \epsilon, \mathbf{V}^{(\ell-1)})$
 - 5: $\mathbf{g}^{(\ell)} = |\tilde{\mathbf{L}}\mathbf{x}^{(\ell)}| / \|\tilde{\mathbf{L}}\mathbf{x}^{(\ell)}\|_\infty$; $\mathbf{d}^{(\ell+1)} = \mathbf{d}^{(\ell)} \circ (1 - \mathbf{g}^{(\ell)})^{os}$
 - 6: **end for**
 - 7: **return** $\mathbf{x}^{(N_{\text{out}})}$
-

Table 3.1 compares iteration structure of edge-preserving methods. Our method achieves cumulative reweighting’s edge quality while maintaining computational efficiency competitive with or better than non-cumulative approaches. The reduction from three to two iteration levels, combined with subspace recycling, provides substantial computational savings, as demonstrated in Section 4.

Table 3.1: Iteration depth comparison of edge-preserving regularization methods. “Levels” counts distinct nested loops; RMM-GKS has one outer loop (enlarge–compress) with no separate inner solver, whereas Kilmer et al.’s projection requires an inner LSQR at each Krylov expansion step.

Method	Cumulative Weighting	Iteration Levels	Subspace Recycling
Standard ℓ_q (RMM-GKS)	No	1	Yes
Cumulative ℓ_2 (Gazzola et al.)	Yes	3	No
CR-ℓ_q-RMM-GKS (ours)	Yes	2	Yes

3.3. Why CR- ℓ_1 -RMM-GKS Outperforms CR- ℓ_2 -RMM-GKS: Complementary Edge-Protection Mechanisms. The consistently superior performance of CR- ℓ_1 -RMM-GKS over CR- ℓ_2 -RMM-GKS admits a clear mechanistic explanation rooted in how each penalty interacts with the cumulative weighting strategy.

In CR- ℓ_2 -RMM-GKS, the ℓ_2 penalty applies uniform smoothing to all gradient components, and edge protection relies *entirely* on the cumulative weight mechanism:

a gradient location at index i is protected only after the cumulative weights have reduced $d_i^{(\ell)}$ sufficiently via the multiplicative update (2.4). Until that detection occurs, ℓ_2 regularization actively suppresses the gradient at that location — potentially erasing soft or ambiguous edges before they can be identified and remembered by the cumulative mechanism.

In contrast, the ℓ_1 penalty is intrinsically sparsity-promoting. Via the MM reweighting (2.2), the effective weight assigned to gradient component i at inner iteration k is

$$(3.2) \quad w_i^{(k)} = \left(|[\mathbf{L}\mathbf{x}^{(k)}]_i|^2 + \epsilon^2 \right)^{-1/2},$$

which for $q = 1$ assigns *larger* penalties to small gradients and *smaller* penalties to large ones. This provides a structural preference for sparse gradient fields that operates regardless of the current cumulative weight state $\mathbf{d}^{(\ell)}$: even before the cumulative weights have identified an edge, the ℓ_1 MM weights already act to preserve large gradient values.

CR- ℓ_1 -RMM-GKS therefore benefits from *two complementary edge-protection mechanisms* acting simultaneously:

1. **Intrinsic sparsity promotion** from the ℓ_1 penalty, which protects large gradients at every inner iteration via the MM weights (3.2), and
2. **Accumulated edge memory** from the cumulative weights, which progressively locks in detected edges across outer iterations via (2.4).

CR- ℓ_2 -RMM-GKS possesses only the second mechanism. This synergy explains two characteristic observations from Section 4: the faster convergence of CR- ℓ_1 -RMM-GKS (edges are protected from the first inner iteration, reducing wasted smoothing before cumulative detection activates) and the pronounced staircase pattern of CR- ℓ_2 -RMM-GKS (many outer cumulative updates are required before edge protection engages, producing the plateau-then-drop behaviour visible in Figures 4.1, 4.3, and 4.5).

4. Numerical Results. We evaluate CR- ℓ_q -RMM-GKS on three representative inverse problems spanning 1D signal recovery and 2D tomographic reconstruction. The experiments demonstrate superior reconstruction quality over standard ℓ_2 , ℓ_1 , and cumulative ℓ_2 baselines, efficient convergence, and scalability across problem sizes and ill-posedness regimes. All experiments highlight **CR- ℓ_1 -RMM-GKS**, which consistently achieves the strongest empirical performance.

Comparison Methods. We compare against: ℓ_2 -**RMM-GKS** (standard Tikhonov regularization (1.2)), ℓ_1 -**RMM-GKS** (non-cumulative MM-GKS with ℓ_1 penalty), and **CR- ℓ_2 -RMM-GKS** (cumulative reweighting with $q = 2$, analogous to Gazzola et al. [7] but using our RMM-GKS solver). All cumulative methods share the same RMM-GKS framework, isolating the effect of the ℓ_q penalty choice.

All experiments are implemented in Python with automatic regularization parameter selection via the discrepancy principle (assuming known noise level $\|\boldsymbol{\eta}\|_2$). Performance is measured by the relative reconstruction error $\text{RRE} = \frac{\|\mathbf{x}_{\text{recon}} - \mathbf{x}_{\text{true}}\|_2}{\|\mathbf{x}_{\text{true}}\|_2}$. Inner iterations terminate when the relative change $\|\mathbf{x}^{(\ell,k+1)} - \mathbf{x}^{(\ell,k)}\|_2 / \|\mathbf{x}^{(\ell,k)}\|_2$ falls below 10^{-5} , with a total iteration budget of 600. For all experiments, we set the cumulative weighting parameter s in (2.4) to 1, and the Krylov subspace dimensions k_{\min} and k_{\max} in Algorithm 2.1 to 5 and 25, respectively.

4.1. Experiment 1: 1D Signal Deblurring. Problem Setup. The goal is to reconstruct a piecewise-constant signal $\mathbf{x}_{\text{true}} \in \mathbb{R}^{200}$ containing sharp jump discon-

tinuities from blurred and noisy observations. The true signal is shown in Figure 4.2.

The forward operator $\mathbf{A} \in \mathbb{R}^{200 \times 200}$ is a Gaussian convolution matrix modeling a blurring point spread function, generated using the TRIPS-PY package [18]. Observed data $\mathbf{b} \in \mathbb{R}^{200}$ are obtained by applying \mathbf{A} to \mathbf{x}_{true} and adding white Gaussian noise $\boldsymbol{\eta}$ with relative noise level $\|\boldsymbol{\eta}\|_2 / \|\mathbf{A}\mathbf{x}_{\text{true}}\|_2 = 0.01$. The noisy blurred signal is shown in the leftmost column of Figure 4.2. This experiment isolates each method’s ability to recover sharp transitions while suppressing noise in smooth regions — a setting where ℓ_1 -type penalties have a well-known structural advantage over ℓ_2 .

Convergence Behavior. Figure 4.1(a) shows RRE versus total iterations. CR- ℓ_1 -RMM-GKS (solid blue) decreases rapidly and achieves the lowest final RRE. CR- ℓ_2 -RMM-GKS (orange dash-dot) exhibits a characteristic *staircase pattern*: each plateau corresponds to an inner RMM-GKS solve, and each drop to an outer cumulative weight update. This reveals that ℓ_2 -type reweighting requires substantially more outer iterations to reach comparable accuracy. Standard ℓ_1 (green dashed) converges quickly initially but stabilizes at a higher error, unable to improve further without the memory of past iterates. Standard ℓ_2 (red dotted) plateaus earliest, as expected from its tendency to oversmooth discontinuities.

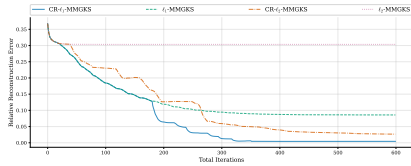
Cumulative Weight Evolution. Figure 4.1(b) illustrates the evolution of cumulative weights (top row) and corresponding reconstructions (bottom row) across outer iterations, providing direct insight into the edge-detection mechanism. Weights near zero indicate detected edges (reduced penalty); weights near one indicate smooth regions.

At the first outer iteration both CR- ℓ_1 - and CR- ℓ_2 -RMM-GKS begin with uniform weights $\mathbf{d}^{(1)} = \mathbf{1}$. By the second iteration, CR- ℓ_1 -RMM-GKS has already identified the major edges as sharp dips in the weight profile, whereas CR- ℓ_2 -RMM-GKS assigns more moderate penalties, producing visible residual smoothing at discontinuities. By the final iteration, CR- ℓ_1 -RMM-GKS has cumulatively locked in all edges: once a discontinuity is detected it remains protected from re-smoothing in subsequent iterations. This history-dependent mechanism is precisely what distinguishes cumulative from non-cumulative reweighting — ℓ_1 -RMM-GKS recomputes weights from the current iterate alone and thus cannot retain edge memory across outer iterations.

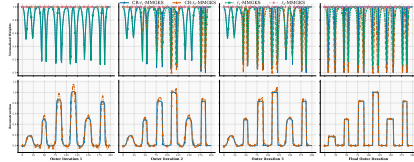
Snapshot Comparison. Figure 4.2 shows final reconstructions after 600 iterations. CR- ℓ_1 -RMM-GKS most closely matches the ground truth, preserving all sharp jumps with minimal overshoot or smoothing. ℓ_2 -RMM-GKS exhibits the most pronounced oversmoothing. ℓ_1 -RMM-GKS and CR- ℓ_2 -RMM-GKS fall between these extremes, with CR- ℓ_1 -RMM-GKS achieving the smallest absolute reconstruction error across the entire signal.

4.2. Experiment 2: Sparse-Angle Computed Tomography. Problem Setup. We now move to a large-scale 2D setting. The goal is to reconstruct a simulated medical phantom image $\mathbf{x}_{\text{true}} \in \mathbb{R}^{16384}$ (reshaped as 128×128) from severely undersampled tomographic projections. The ground truth is the Shepp–Logan phantom, a standard benchmark in medical imaging whose elliptical regions with sharp intensity boundaries represent idealized tissue interfaces (see Figure 4.4).

The forward operator $\mathbf{A} \in \mathbb{R}^{5430 \times 16384}$ is a Radon transform matrix for fan-beam X-ray projections at only 30 equidistant angles in $[0^\circ, 180^\circ]$ [15]. Standard clinical tomography requires 180 or more projection angles for artifact-free reconstruction; our 30-angle setup is thus severely ill-posed. Observed data $\mathbf{b} \in \mathbb{R}^{5430}$ (the *sinogram*) are obtained by applying \mathbf{A} to the vectorized phantom and adding white Gaussian noise at a relative level of 1%. This experiment tests whether cumulative reweighting



(a) Relative reconstruction error versus total iterations. CR- ℓ_1 -RMM-GKS (blue solid) achieves lowest error.



(b) Evolution of cumulative weights (top row) and reconstructions (bottom row) across outer iterations.

Fig. 4.1: **Experiment 1: 1D deblurring.** CR- ℓ_1 -RMM-GKS achieves the lowest RRE and stabilizes faster than competing methods through cumulative edge memory.

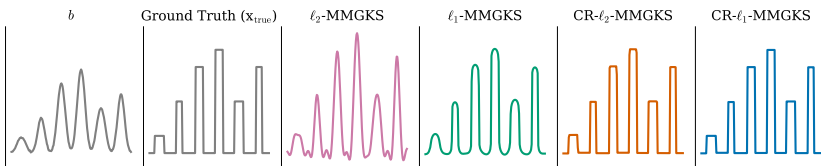


Fig. 4.2: **Experiment 1: Final reconstructions after 600 iterations.** Left to right: noisy blurred data \mathbf{b} , ground truth \mathbf{x}_{true} , and reconstructions from ℓ_2 -RMM-GKS, ℓ_1 -RMM-GKS, CR- ℓ_2 -RMM-GKS, and CR- ℓ_1 -RMM-GKS. CR- ℓ_1 -RMM-GKS best preserves sharp jumps with minimal smoothing artifacts.

retains its advantage as problem scale increases and preserving anatomical boundaries becomes the central challenge.

Convergence Behavior. Figure 4.3 shows RRE versus total iterations. The qualitative picture mirrors Experiment 1: CR- ℓ_1 -RMM-GKS achieves the lowest final RRE and descends most rapidly, while CR- ℓ_2 -RMM-GKS displays the same staircase pattern, here requiring noticeably more outer iterations to make progress. Standard ℓ_1 again plateaus at an intermediate error, and standard ℓ_2 flattens earliest. Importantly, the performance gap between cumulative and non-cumulative methods is more pronounced here than in the 1D case, suggesting that cumulative edge memory becomes increasingly valuable as problem dimension and ill-posedness grow. Although both CR methods reach the same final RRE of 0.101 at the 600-iteration budget, CR- ℓ_1 -RMM-GKS achieves this level markedly earlier, as is evident from Figure 4.3; the advantage of cumulative ℓ_1 reweighting thus lies in convergence speed as much as in final accuracy for this problem.

Snapshot Comparison. Figure 4.4 presents final reconstructions after 600 iterations. CR- ℓ_1 -RMM-GKS produces the sharpest boundaries between tissue regions, closely matching the ground truth ellipse edges. Standard ℓ_2 shows significant blurring that obscures these boundaries, while ℓ_1 -RMM-GKS and CR- ℓ_2 -RMM-GKS recover intermediate levels of detail. The qualitative ranking is consistent with the RRE curves.

4.3. Experiment 3: Limited-Angle Computed Tomography. Problem Setup. The final experiment addresses a qualitatively different form of ill-posedness.

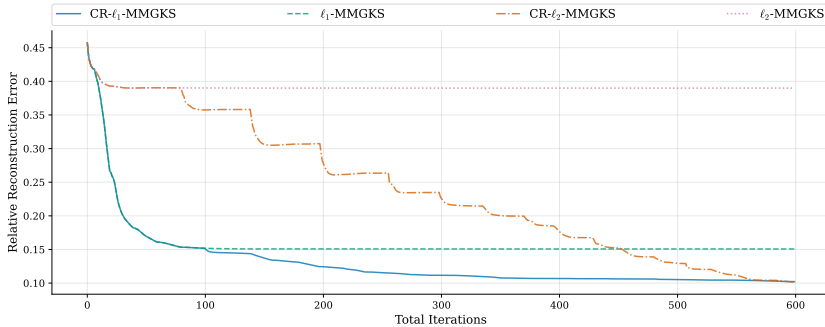


Fig. 4.3: **Experiment 2: Convergence.** CR- ℓ_1 -RMM-GKS converges smoothly to the lowest error. CR- ℓ_2 -RMM-GKS shows a pronounced staircase, requiring more outer iterations; standard ℓ_2 flattens earliest due to oversmoothing.

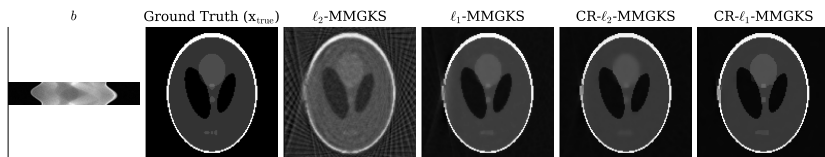


Fig. 4.4: **Experiment 2: Final reconstructions after 600 iterations.** Left to right: sinogram \mathbf{b} , ground truth \mathbf{x}_{true} , and reconstructions from ℓ_2 -RMM-GKS, ℓ_1 -RMM-GKS, CR- ℓ_2 -RMM-GKS, and CR- ℓ_1 -RMM-GKS. CR- ℓ_1 -RMM-GKS produces the sharpest tissue boundaries; ℓ_2 -RMM-GKS exhibits significant blurring of anatomical interfaces.

Rather than reducing the number of projection angles uniformly over $[0^\circ, 180^\circ]$, we restrict the angular range entirely, acquiring projections only within a narrow cone. The goal is to reconstruct $\mathbf{x}_{\text{true}} \in \mathbb{R}^{4096}$ (reshaped as 64×64) from this angularly incomplete data. The ground truth is the tectonic phantom [18], a test image featuring layered structures with sharp structural boundaries (see Figure 4.6).

The forward operator $\mathbf{A} \in \mathbb{R}^{5460 \times 4096}$ encodes fan-beam projections at 60 equidistant angles restricted to $[0^\circ, 60^\circ]$ — only one third of the full angular sweep. Features whose dominant gradients align with unmeasured directions are invisible to \mathbf{A} , making recovery dependent almost entirely on the regularizer’s structural assumptions. Observed data $\mathbf{b} \in \mathbb{R}^{5460}$ are obtained as before, with a relative noise level of 0.5%. This lower noise level reflects the focus on geometric ill-posedness rather than measurement corruption, allowing a cleaner comparison of how each regularizer handles the missing-angle problem.

Convergence Behavior. Figure 4.5 shows RRE versus total iterations. CR- ℓ_1 -RMM-GKS converges to a markedly lower final RRE than in Experiment 2, consistent with the lower noise level and the strong sparsity-promoting structure of ℓ_1 reweighting on piecewise-smooth phantoms. The staircase in CR- ℓ_2 -RMM-GKS remains visible, and the gap between CR- ℓ_1 - and CR- ℓ_2 -RMM-GKS is wider than in the sparse-angle case, indicating that cumulative ℓ_1 reweighting is especially well-suited to the piecewise-flat geometry of the tectonic phantom. Standard ℓ_2 flattens at a high

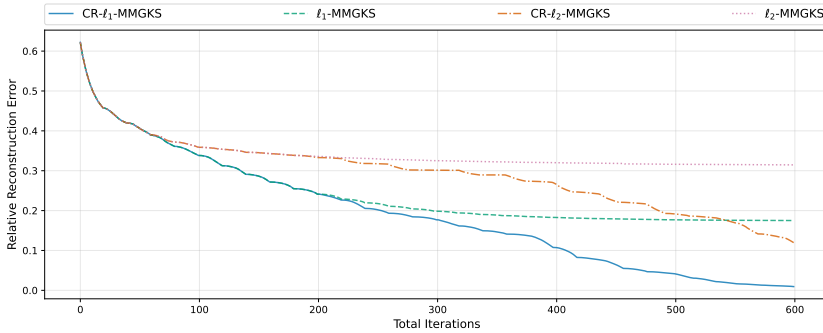


Fig. 4.5: **Experiment 3: Convergence.** CR- ℓ_1 -RMM-GKS converges smoothly to the lowest error. CR- ℓ_2 -RMM-GKS shows a staircase pattern; standard ℓ_2 flattens at a high RRE plateau, reflecting its failure to resolve the limited-angle geometry.

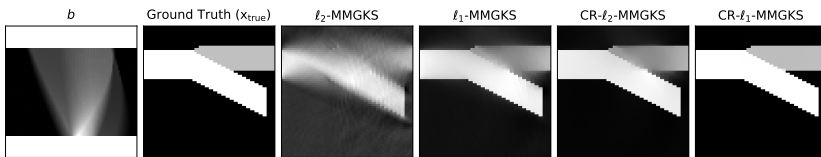


Fig. 4.6: **Experiment 3: Final reconstructions after 600 iterations.** Left to right: sinogram \mathbf{b} , ground truth \mathbf{x}_{true} , and reconstructions from ℓ_2 -RMM-GKS, ℓ_1 -RMM-GKS, CR- ℓ_2 -RMM-GKS, and CR- ℓ_1 -RMM-GKS. Streak artifacts from the missing angular range are prominent in ℓ_2 -RMM-GKS and substantially suppressed by CR- ℓ_1 -RMM-GKS.

error plateau, consistent with its inability to resolve the sharp directional boundaries that define this phantom.

Snapshot Comparison. Figure 4.6 shows final reconstructions after 600 iterations. The limited-angle geometry produces distinctive streak artifacts in the ℓ_2 -RMM-GKS reconstruction. CR- ℓ_1 -RMM-GKS substantially suppresses these artifacts and recovers the sharpest approximation to the true boundary structure. ℓ_1 -RMM-GKS and CR- ℓ_2 -RMM-GKS achieve partial suppression, falling between the two extremes and confirming that both the cumulative mechanism and the ℓ_1 penalty contribute independently to artifact reduction.

4.4. Summary of Findings. Across all three experiments, the results support three consistent conclusions. First, cumulative reweighting outperforms its non-cumulative counterpart regardless of the penalty choice: both CR- ℓ_1 - and CR- ℓ_2 -RMM-GKS achieve better edge preservation than ℓ_1 - and ℓ_2 -RMM-GKS respectively, confirming that retaining edge memory across outer iterations is a meaningful structural advantage. Second, the ℓ_1 penalty and cumulative reweighting are *synergistic*: CR- ℓ_1 -RMM-GKS consistently outperforms CR- ℓ_2 -RMM-GKS in both convergence speed and final reconstruction quality, demonstrating that the two mechanisms reinforce rather than duplicate each other. Third, this improved quality does not come at a computational cost: despite the added overhead of cumulative weight updates, CR-

ℓ_1 -RMM-GKS converges in a comparable number of total iterations to ℓ_1 -RMM-GKS, and substantially fewer than CR- ℓ_2 -RMM-GKS.

Table 4.1: Quantitative reconstruction results (RRE) after 600 iterations. Best results per experiment in **bold**.[†]

Method	Experiment 1	Experiment 2	Experiment 3
ℓ_2 -RMM-GKS	0.304	0.390	0.315
ℓ_1 -RMM-GKS	0.086	0.151	0.175
CR- ℓ_2 -RMM-GKS	0.026	0.101	0.108
CR- ℓ_1 -RMM-GKS	0.004	0.101	0.007

[†]In Experiment 2, CR- ℓ_1 - and CR- ℓ_2 -RMM-GKS reach the same final RRE within the 600-iteration budget; CR- ℓ_1 -RMM-GKS is preferred on the basis of faster convergence (see Figure 4.3).

5. Conclusion. We introduced CR- ℓ_q -RMM-GKS, a framework that combines cumulative spatial reweighting with Krylov subspace recycling for edge-preserving image reconstruction. The framework reduces the deeply nested iteration structure of prior cumulative methods from three levels to two, extends cumulative weighting to general ℓ_q penalties, and retains automatic regularization parameter selection. Numerical experiments in 1D signal deblurring, sparse-angle tomography, and limited-angle tomography consistently show that CR- ℓ_1 -RMM-GKS achieves the lowest reconstruction error and sharpest boundaries among all compared methods, and that the cumulative mechanism and the ℓ_1 penalty are synergistic rather than redundant.

Several limitations point toward future work. First, a formal convergence theory for the outer cumulative loop remains open. Second, the cumulative weighting parameter s and the Krylov dimensions k_{\min} , k_{\max} are currently set by hand; adaptive or problem-driven selection rules would improve deployability.

6. Acknowledgments. M.P. gratefully acknowledges support from NSF DMS under award No. 2410699. T.O. and M.K. acknowledge support from NSF DMS No. 2410698. Any opinions, findings, conclusions, or recommendations expressed in this material are those of the authors and do not necessarily reflect the views of the National Science Foundation.

REFERENCES

- [1] C. ATKINSON, *Methods for solving incorrectly posed problems*, Bulletin of the London Mathematical Society, 17 (1985), pp. 621–622, <https://doi.org/https://doi.org/10.1112/blms/17.6.621>, <https://londmathsoc.onlinelibrary.wiley.com/doi/abs/10.1112/blms/17.6.621>, <https://arxiv.org/abs/https://londmathsoc.onlinelibrary.wiley.com/doi/pdf/10.1112/blms/17.6.621>.
- [2] J. M. BARDSLEY, *Laplace-distributed increments, the Laplace prior, and edge-preserving regularization*, Journal of Inverse and Ill-Posed Problems, 20 (2012), pp. 271–285.
- [3] S. BOYD, N. PARIKH, E. CHU, B. PELEATO, AND J. ECKSTEIN, *Distributed optimization and statistical learning via the alternating direction method of multipliers*, Foundations and Trends in Machine Learning, 3 (2011), pp. 1–122, <https://doi.org/10.1561/22000000016>.
- [4] E. J. CANDÈS, M. B. WAKIN, AND S. P. BOYD, *Enhancing sparsity by reweighted ℓ_1 minimization*, Journal of Fourier Analysis and Applications, 14 (2008), pp. 877–905.
- [5] J. CHUNG AND A. K. SAIBABA, *Generalized hybrid iterative methods for large-scale Bayesian inverse problems*, SIAM Journal on Scientific Computing, 39 (2017), pp. S24–S46.

- [6] I. DAUBECHIES, R. DEVORE, M. FORNASIER, AND C. S. GÜNTÜRK, *Iteratively reweighted least squares minimization for sparse recovery*, Communications on Pure and Applied Mathematics, 63 (2010), pp. 1–38.
- [7] S. GAZZOLA, M. E. KILMER, AND P. C. HANSEN, *A cumulative reweighted ℓ_2 method for edge-preserving regularization*, SIAM Journal on Scientific Computing, 42 (2020), pp. B1015–B1038.
- [8] T. GOLDSTEIN AND S. OSHER, *The split Bregman method for L_1 -regularized problems*, SIAM Journal on Imaging Sciences, 2 (2009), pp. 323–343, <https://doi.org/10.1137/080725891>.
- [9] P. C. HANSEN, *Analysis of discrete ill-posed problems by means of the L -curve*, SIAM Review, 34 (1992), pp. 561–580.
- [10] P. C. HANSEN, *Discrete Inverse Problems: Insight and Algorithms*, SIAM, Philadelphia, 2010.
- [11] G. HUANG, A. LANZA, S. MORIGI, L. REICHEL, AND F. SGALLARI, *Majorization–minimization generalized Krylov subspace methods for ℓ_p - ℓ_q optimization applied to image restoration*, BIT Numerical Mathematics, 57 (2017), pp. 351–378.
- [12] D. R. HUNTER AND K. LANGE, *A Tutorial on MM Algorithms*, The American Statistician, 58 (2004), pp. 30–37.
- [13] M. E. KILMER, P. C. HANSEN, AND M. I. ESPAÑOL, *A projection-based approach to general-form Tikhonov regularization*, SIAM Journal on Scientific Computing, 29 (2007), pp. 315–330.
- [14] K. LANGE, *The MM Algorithm*, Springer New York, New York, NY, 2004, pp. 119–136.
- [15] F. NATTERER, *The Mathematics of Computerized Tomography*, SIAM, Philadelphia, 2001.
- [16] T. OKUNOLA, M. PASHA, M. KILMER, AND M. FREITAG, *Efficient dynamic image reconstruction with motion estimation*, 2025, <https://arxiv.org/abs/2501.12497>.
- [17] M. PASHA, E. DE STURLER, AND M. E. KILMER, *Recycling MMGKS for large-scale dynamic and streaming data*, 2023, <https://arxiv.org/abs/2309.15759>.
- [18] M. PASHA, S. GAZZOLA, C. SANDERFORD, AND U. O. UGWU, *TRIPs-Py: Techniques for regularization of inverse problems in Python*, Numerical Algorithms, (2024), pp. 1–38.
- [19] P. RODRIGUEZ AND B. WOHLBERG, *Efficient minimization method for a generalized total variation functional*, IEEE Transactions on Image Processing, 18 (2009), pp. 322–332.
- [20] L. I. RUDIN, S. OSHER, AND E. FATEMI, *Nonlinear total variation based noise removal algorithms*, Physica D: Nonlinear Phenomena, 60 (1992), pp. 259–268.
- [21] B. WOHLBERG AND P. RODRIGUEZ, *An iteratively reweighted norm algorithm for minimization of total variation functionals*, IEEE Signal Processing Letters, 14 (2007), pp. 948–951.